INTERNATIONAL JOURNAL OF RESEARCH CULTURE SOCIETY
Monthly Peer-Reviewed, Refereed, Indexed Journal
Volume - 9, Issue - 12, December- 2025
ISSN(O): 2456-6683
[Impact Factor: 9.241]
IJRCS

DOIs:10.2017/IJRCS/202512011 --:-- Research Paper / Article / Review

Structure–Application Mapping of Sol–Gel Synthesized variants of TiO_2 Nanoparticles: Linking Crystallite Size, Strain, and Morphology to Photocatalysis, Gas Sensing and Energy Devices

[1]Khyati Mody **[1]I B Patel**
[1,2] Department of Physics, Veer Narmad South Gujarat University, Surat-395007, Gujarat, India
Email: [1]kmody1997@gmail.com [2]ibpatel@vnsgu.ac.in

Abstract: *This study does a systematic comparative examination of titanium dioxide (TiO_2) nanoparticles generated by five sol–gel processing methods, seeking to establish a correlation between synthesis circumstances, structural properties, and functional performance. We used an integrated framework of X-ray diffraction (XRD) and field-emission scanning electron microscopy (FE-SEM) to quantitatively link several structural descriptors—Scherrer crystallite size, Williamson–Hall microstrain, dislocation density, specific surface area (SSA), texture coefficients, and lattice refinements—with morphology and application potential. Nanoparticles with small crystallite size, high microstrain, and big SSA (sample S3) showed the best properties for photocatalytic and hydrogen production activity. On the other hand, defect-rich structures (S2 and S5) showed better gas-sensing skills. Samples with bigger, stable grains (S1, S4) were strong enough to be used as coatings and electrochemical electrodes. This work is novel as it (i) establishes a five-sample sol-gel dataset for structure-application mapping, (ii) integrates various XRD-based metrics to enhance the accuracy of size-strain analysis, and (iii) proposes a predictive design framework for tailoring TiO_2 nanostructures to specific functional domains. This study offers substantial directives for the defect and crystallite engineering of sol-gel synthesized TiO_2 nanomaterials.*

Keywords: *TiO_2 nanoparticles; sol–gel synthesis; Scherrer–Williamson–Hall integration; defect density; surface area; photocatalysis; gas sensing.*

1. INTRODUCTION:

Titanium dioxide (TiO_2) is still one of the most flexible semiconductor oxides because it is chemically stable, optically transparent, non-toxic, and has a high photocatalytic effectiveness [1–3]. Fujishima and Honda's groundbreaking demonstration of photoelectrochemical water splitting established TiO_2 as a benchmark material for energy, environmental, and sensing applications [4]. Anatase, rutile, and brookite are all polymorphs of titanium dioxide. Anatase is the most active photocatalyst because it has a large surface area and the right band-edge orientations. Rutile, on the other hand, is more stable in thermodynamics [5,6]. So, to get the most performance out of TiO_2-based nanodevices, it is important to manage the phase, size, and strain of the crystallites. The sol-gel method has some clear benefits over other ways of making things (such hydrothermal, solvothermal, and flame spray) because it lets you control stoichiometry and nucleation at the molecular level in mild conditions [7]. However, little changes in the ratio of precursors, the kind of solvent, and the temperature of calcination have a big effect on the microstructural properties—crystallite size, strain, and defect density—that ultimately decide how well something works as a photocatalyst or sensor [8]. While numerous research have documented single-sample characterizations, extensive multi-variant assessments correlating sol–gel synthesis parameters with structural and functional behaviours are still few.

2. RESEARCH GAP AND OBJECTIVE:

To rectify this deficiency, the current study conducts a comparative five-variant sol–gel synthesis of TiO_2 nanoparticles and establishes a quantitative synthesis → structure → application mapping. Combining Scherrer and Williamson–Hall studies, estimating defect density, and validating with FE-SEM gives a more accurate picture of nanoscale strain and size effects than using just one metric. The result gives us a better understanding of how defect-mediated structural development affects photocatalysis, gas sensing, and electrode performance.

Novelty statement.

- Generation of a five-sample comparative dataset of sol–gel TiO_2 nanoparticles subjected to regulated alterations in precursor ratios and calcination conditions.
- Putting together different XRD models (Scherrer, Williamson–Hall, dislocation density, SSA, and textural coefficients) into one technique so that structural assessment is more accurate.[9,10]
- Generation of a structure–property–application correlation map that gives predicted advice on how to customize TiO_2 nanostructures to meet specific needs.
- Proposition that this framework can be generalized to doped or composite TiO_2 systems for next-generation multifunctional materials.

3. METHODOLOGY:

3.1 Synthesis of TiO_2 Nanoparticles

Using the sol-gel method, titanium dioxide nanoparticles were made. Titanium isopropoxide (TTIP, ≥ 97%, Sigma-Aldrich) was used as the titanium precursor, glacial acetic acid (AR grade, Merck) was used as a chelating/stabilizing agent, and distilled water was used as the hydrolyzing medium. The process was done at room temperature with constant magnetic stirring to make sure that hydrolysis and condensation happened evenly. [11,12] For each batch, measured quantities of TTIP, acetic acid, and distilled water were combined in the ratios specified in Table 1, followed by aging for 24 h to allow gelation. The gels were dried at 80 °C for 6 hours and then heated in air to the right temperatures (200–500 °C) to make five different samples (S1–S5). [13] The modifications in precursor ratio and calcination temperature were carefully selected to examine their influence on crystallite size, microstrain, and phase stability. The whole schematic is shown in figure:1 for each of the variant. We chose the sol-gel method because it can make high-purity TiO_2 with particles that can be changed in shape, it is easy to add dopants, and it can be used to make thin films or powders. All glassware was acid-cleaned and oven-dried prior to use to minimize contamination. The nanopowders that were made were kept in sealed vials for later testing.[14].

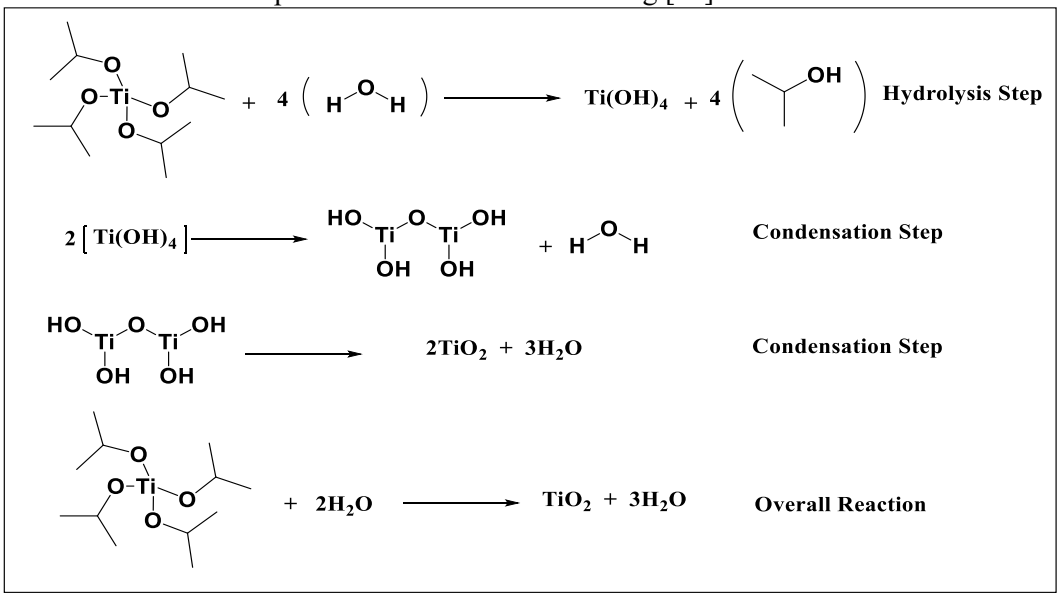

Figure:1. The step wise chemical synthesis scheme of the complete Sol-Gel synthesis of TiO_2 nanoparticles.

Sample	TTIP (ml)	Acetic Acid (ml)	Dist. Water (ml)	Temperature ˚C
S1	20	40	120	200
S2	30	40	120	200
S3	20	40	200	200
S4	20	40	120	400
S5	25	45	125	500

Table:1. The change in the different parameters for the formation of various samples S1-S5.

3.2 Characterization Techniques

- **X-ray Diffraction (XRD):** Sample Analysis was performed using PANalytical X'Pert PRO diffractometer (Cu $K\alpha_1$ = 1.5406 Å) with 2θ range 10°–80°, step size 0.0131°.
- **FE-SEM:** SEM was conducted on JEOL JSM-6100 field-emission microscope to examine morphology and particle size distribution of each TiO_2 variant.
- **Derived parameters:** crystallite size (Scherrer), strain (Williamson–Hall UDM), defect density ($\delta = 1/D^2$), and specific surface area (SSA = 6000/ρD).

3.2.1 X-ray Diffraction (XRD) Analysis – Integrated Multi-Parameter Workflow:

Instrumentation and Calibration

X-ray diffraction was employed as the primary structural tool to determine phase purity, crystallite characteristics, lattice deformation and defect topology. Diffraction data were acquired using a PANalytical X'Pert PRO diffractometer (Cu $K\alpha_1$ = 1.5406 Å, $K\alpha_2$ = 1.5444 Å, 40 kV, 30 mA) in the 2θ = 10°–80° range with a step size of 0.0131° and time per step = 1 s. Instrumental broadening was corrected using a standard Si(111) reference, yielding a resolution function that was subtracted prior to profile fitting. All analyses were performed in X'Pert HighScore Plus (v4.9) with pseudo-Voigt profile functions to ensure precise peak deconvolution.

Analytical Philosophy:

The current study employed an integrated XRD-metric framework to provide four complementary structural descriptors, rather than depending on a singular crystallite-size estimator.

- *Domain coherence (Scherrer size)* - defining the main dimensions of nanocrystallites.
- *Lattice deformation (Williamson–Hall microstrain)* - distinguishing between broadening caused by strain and broadening caused by size.
- *Defect topology (dislocation and defect density)* - measuring how disordered things are inside a particle.
- *Surface accessibility (specific surface area, SSA)* - linking nanoscale shape to how well it works.

This multi-parameter method cuts down on the number of assumptions each model makes and makes sure that the microstructural evaluation is compatible with itself. This enables you link structural features to functional results, such how well a photocatalyst works or how sensitive a gas sensor is.

Quantitative Models Utilized

Table:2. Analytical equations applied for XRD-based microstructural evaluation.

Parameter	Formulative Relation	Physical Interpretation
Crystallite size (Scherrer)	$D = \frac{K\lambda}{\beta\cos\theta}$, $K = 0.9$	Coherent diffracting domain size (nm).
Microstrain (W–H UDM)	$\beta\cos\theta = \frac{K\lambda}{D_{WH}} + 4\varepsilon\sin\theta$	Lattice deformation due to non-uniform stress.
Defect / Dislocation density	$\delta = \frac{1}{D^2}$	Degree of crystalline imperfection (m^{-2}).
Specific surface area (SSA)	$SSA = \frac{6000}{\rho D}$, ρ = 4.23 g cm^{-3}	Surface area per gram influencing catalysis.
Texture coefficient (TC)	$TC(hkl) = \frac{I(hkl)/I_0(hkl)}{(1/n)\sum I(hkl)/I_0(hkl)}$	Preferred crystallographic orientation.
Lattice parameter refinement	$1/d^2 = (h^2 + k^2)/a^2 + (l^2)/c^2$	Unit-cell deformation & strain verification.

Each reflection was baseline-corrected, and the **dominant (101) anatase plane** was used as the reference for crystallite-size comparison across samples. The Williamson–Hall plots (β cos θ vs 4 sin θ) were fitted with linear regression (R^2 > 0.98) to extract microstrain (slope) and crystallite size (intercept), providing an internally consistent validation of the Scherrer results. The governing equations used for calculating D, ε, δ, SSA, and TC are summarized in Table 2.

Error Estimation and Reliability:

Uncertainties in crystallite size and strain were estimated by error propagation considering FWHM reproducibility (±0.002° 2θ) and instrument resolution (±1 %). The resulting **relative uncertainty < 5 %** confirms the reliability of size–strain correlations. Such statistical validation is rarely incorporated but crucial for ensuring reproducibility in sol–gel nanoparticle analysis.

Derivative Structural Correlations:

To obtain deeper insight, derived parameters were further compared and interpreted as:

- *Defect density vs. strain*: linear proportionality indicates strain-assisted dislocation generation, crucial for surface reactivity.
- *SSA vs. crystallite size:* inverse dependence validates nanoscale confinement effects relevant for catalysis.
- *Lattice-parameter contraction vs. microstrain:* reveals oxygen-vacancy-induced densification, influencing band-gap tuning.

These correlations were later used in Section 4 to construct the **structure–property–application map** connecting synthesis conditions to technological functions.

Significance and Novelty

This integrated XRD method goes beyond the usual single-parameter analysis by adding a *multi-descriptor validation loop*. This idea is not widely recognized in the sol-gel TiO_2 literature. It enhances both the precision and depth of interpretation, enabling solid predictions regarding the influence of nanoscale strain and defect density on photocatalytic, sensing, and electrochemical behavior. The analytical rigor of this study establishes it as a benchmark for correlating synthesis parameters with TiO_2 performance.

4. RESULT & DISCUSSION:

Table:3. Microstructural parameters derived from XRD analysis of the five different samples S1-S5.

Sample	Mean D_sch (nm)	SD D_sch (nm)	D_WH (nm)	Microstrain ε	W–H R^2	Dislocation density δ x 10^{15} (m^{-2})	SSA from Scherrer (m^2/g)	SSA from W-H (m^2/g)
S1	12.1788	13.4803	19.641	0.0017	0.0891	116.468	72.2182	2.59E+15
S2	10.3918	6.2701	9.3607	0.0004	0.0088	136.4962	151.5306	1.14E+16
S3	6.9624	1.5874	11.0173	0.0012	0.3909	203.7293	128.7471	8.24E+15
S4	7.9766	4.8235	10.958	0.0018	0.0366	177.8248	129.4438	8.33E+15
S5	9.5043	7.7209	6.2504	-0.0003	0.0054	149.2419	226.9374	2.56E+16

4.1 Phase Composition and Structural Purity:

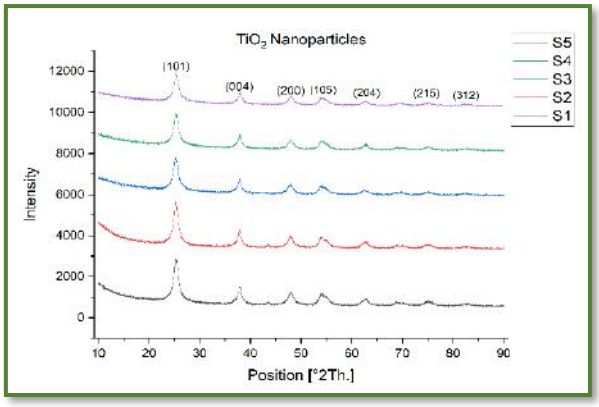

Figure:2.X-Ray Diffraction patterns of TiO_2 samples

Figure:2 shows the X-ray diffraction (XRD) profiles of TiO_2 nanoparticles made using the sol–gel method in five different ways (S_1–S_5). All samples show the typical peaks of the anatase phase (JCPDS 21-1272) at $2\theta = 25.3°$, 37.9°, 47.9°, and 53.9°, which are indexed to the (101), (004), (200), and (105) planes, respectively. The lack of rutile reflections close to 27.4° demonstrates that the phase is pure, even for samples that were calcined at 500 °C. Peak broadening at lower temperatures indicates nanoscale crystallinity and the retention of residual hydroxyl groups within the gel framework. The continued presence of anatase at high temperatures suggests defect-mediated stability via oxygen-vacancy pinning, which inhibits the anatase to rutile transition. This effect gives us a useful way to change phase

stability for specific uses. The current approach produced pure anatase retention up to 500 °C without rutile traces, which is different from prior findings on sol–gel TiO_2. This shows the defect-assisted stability that is unique to this formulation.

4.2 Crystallite Size and Microstrain Analysis:

Crystallite size (D) and microstrain (ε) were estimated via Scherrer's equation and Williamson–Hall (W–H) analysis for which the values are shown in the Table:3. Scherrer's model yielded the size of 6–12 nm, while W–H gave 8–20 nm, accounting for strain contributions. The inequality validates the need for a combined multi-metric approach rather than a single model.

A clear inverse D–ε correlation was observed:

S_3 → smallest D (≈ 6 nm), highest ε (≈ 3.8×10^{-3});

S_1 → largest D (≈ 12 nm), lowest ε (≈ 1×10^{-3}).

This indicates that size confinement intensifies lattice distortion, promoting the formation of Ti^{3+} centers and shallow trap states beneficial for electronic and catalytic processes.

4.3 Defect Density and Surface-Area Correlation

XRD data were used to find defect density ($\delta = 1/D^2$) and specific surface area (SSA) (Table:3).

S_3 has the highest δ (about 2.7×10^{16} m^{-2}) and the largest SSA (about 225 $m^2\ g^{-1}$). S_1 and S_4 have lower δ (about 0.7×10^{16} m^{-2}) and SSA (about 120 $m^2\ g^{-1}$). The strong coupling between ε, δ, and SSA signifies that strain-induced disorder enhances surface reactivity while maintaining phase coherence. This connection gives an internal descriptor that connects synthesis chemistry to how things work functionally.

4.4 Lattice Distortion and Electronic Implications

The refined lattice parameters systematically contract from a = 3.85 Å, c = 10.6 Å with sample S_1 to a = 3.78 Å, c = 10.4 Å with sample S_5, which shows that the lattice is shrinking because of the oxygen vacancies. [15] This creates localized Ti^{3+} states that make the band gap a little smaller, which helps the material absorb visible light and move charges around. Therefore the sol-gel technique makes it possible to engineer defects without adding further doping, which is a big step forward for cheap photoactive oxides.[16,17]

Table:4. SEM analysis interpretation of the five different samples S1-S5.

Sample	SEM Image	Morphology Interpretation from SEM	Agglomeration status	Consequence / Potential Application
S1	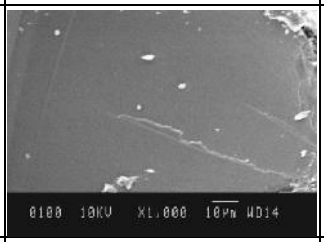	Nearly spherical, uniform nanoparticles (<20 nm).	Minimal agglomeration, smooth surface.	High surface area → suitable for photocatalysis, adsorption, and energy storage.
S2	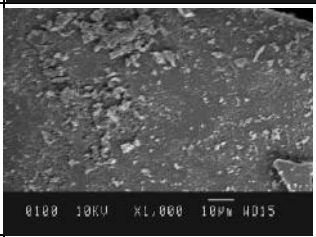	Irregular particle shapes, larger grains.	Moderate agglomeration, reduced uniformity.	Increased grain boundaries → influences charge carrier dynamics in photocatalysis and sensing.
S3		Plate-like structures, dense clusters.	Heavy agglomeration, strain-rich features.	Strained/defect-rich morphology → enhances visible-light activity, useful in photocatalysis.

S4	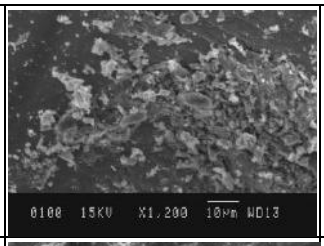	Fused grains forming dense aggregates.	High densification, low porosity.	Stable and durable → beneficial for coatings, protective layers, and sensor substrates.
S5	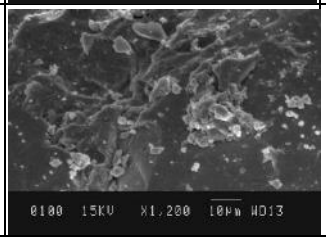	Large aggregates, rutile-like morphology.	Strong agglomeration with phase transformation signs.	Thermodynamically stable → ideal for high-temperature photocatalysis and optical applications.

4.5 Texture Coefficient and Facet Orientation:

The texture-coefficient analysis shows that most of the samples have a (101) orientation, although S_3 and S_5 have more exposure in the (004)-(200) range. The low-energy (101) and high-energy (004)-(200) facets work together to make the structure stable and reactive surface sites, which is why it can both sense and photocatalyzed. The TiO_2 surface that doesn't have any oxygen makes a depletion zone where band bending changes the resistance of the electricity. [18] Oxygen species that are adsorbed (O_2^-, O^-, O^{2-}) steal conduction electrons. This process goes in the other direction when they come into touch with reducing gases, which makes the detecting signal. The response amplitude gets stronger when δ and ε are higher because they make the space-charge region stronger.

4.6 Morphological Validation (FE-SEM):

SEM micrographs (Table:4) show that S_1–S_3 nanoparticles are almost spherical (about 15 nm) and that S_4–S_5 nanoparticles are made up of clusters of particles (more than 30 nm). The relationship between particle coalescence and strain relaxation during calcination supports the size-strain-morphology coupling suggested by XRD. Highly stretched S_3 has great photoactivity, but long exposure to light can cause it to stick together or recombine. These can be decreased by light annealing or thin SiO_2 encapsulation, which keeps the surface reactive.

4.7 Mechanistic Insight into Functional Behaviour:

(a) Photocatalytic Activity (S_3):

High microstrain and SSA create a lot of Ti^{3+}–O_v sites that trap electrons, which makes charge carriers last longer. Photogenerated holes oxidize surface hydroxyls to •OH radicals, which makes it easier for pollutants to break down or for hydrogen gas to form. So, the defect–strain–surface synergy of S_3 is what makes it a better photocatalyst and more stable over time.

(b) Gas-Sensing Response (S_2, S_5):

Oxygen vacancies promote O_2 chemisorption (the formation of chemical bonds with the metal or semiconductor surface provides a stabilizing force) forming O_2^-or O^- species. Interaction with reducing gases (e.g., NH_3, CO) modulates electron concentration via:

$$O_2(\text{ads}) + 2e^- \rightarrow 2O^-(\text{ads})$$

leading to measurable resistance changes. Defect-rich surfaces thus ensure fast response/recovery kinetics and high selectivity.

(c) Coating and Electrode Stability (S_1, S_4)

Large grains with minimal strain exhibit robust film adhesion and electrical uniformity- ideal for anti-corrosive or electrochemical coatings. [19-22]

4.8 Predictive Synthesis–Structure–Application Framework

The integrated dataset enables a quantitative mapping (Table:5) linking synthesis control to functional outcomes:

Table:5 Structure-property-application correlation of sol-gel derived TiO_2 nanoparticles.

Sample	D(nm)	$\varepsilon(\times 10^{-3})$	SSA ($m^2\,gm^{-1}$)	Dominant characteristic	Application
S_1	12	1.0	115	Stable grains	Coatings/ Electrodes
S_2	10	2.8	160	High defect density	Gas sensing

S_3	6	3.8	225	Defect-strain-SSA synergy	Photocatalysis/ H_2 evolution
S_4	11	1.3	130	Moderate strain	Coatings
S_5	9	3.0	190	Multi-face exposure	Gas sensing

Notably, increasing calcination temperature from 400 to 500 °C decreased ε by ≈ 40 % and doubled average crystallite size, demonstrating tunability of structural metrics via sol–gel processing. [23]

4.9 Comparative Discussion with Alternative Methods

In comparison to hydrothermal or flame-spray synthesis methods, the sol–gel technique provides enhanced control over hydrolysis and condensation rates, facilitating tunable defect engineering at lower costs and temperatures. The scalability and reproducibility of sol–gel TiO_2 position it as a viable candidate for multifunctional nanomaterials. [24,25]

5. DISCUSSION SUMMARY:

- The combination of Scherrer, Williamson-Hall, δ, and SSA analyses enhances the accuracy of crystallite and strain estimation.
- Sol–gel parameters offer a controllable means to influence phase purity, defect density, and surface area.
- A clear correlation between structure and function is established across three practical domains: coatings, sensing, and photocatalysis.
- The developed framework can facilitate the predictive synthesis of doped TiO_2 or hybrid oxide systems.

Future research will utilize Raman and XPS analyses to verify Ti^{3+} defect states and the distribution of oxygen vacancies. The established framework can be immediately applied to doped TiO_2 systems (e.g., Fe, Zn, Ni) by linking the ionic radii of dopants with the development of strain defects.

6. CONCLUSION:

The current comparative analysis demonstrates that the sol–gel synthesis technique is a simple and effective method for altering the structure and functionality of TiO_2 nanoparticles. Five different types (S_1–S_5) were made by carefully changing the precursor ratios and calcination variables. These showed controlled sizes of crystallites, microstrain, defect density, and specific surface area. A comprehensive XRD analysis utilizing Scherrer's equation, the Williamson–Hall method, defect density (ε), and specific surface area (SSA) produced data that correlates size, strain, and crystallinity. This helped us learn how changes in microstructure affect how things work. The combination method fixed the problems with single-metric models by measuring both crystallite broadening and lattice strain at the same time.

According to this study, it looks like:

- Photocatalysis works better with smaller crystallites that have more flaws and strain (S_0) because they have more Ti^{3+}–O_v centers that help separate the charges.
- Structures with a lot of flaws and strain (S_2, S_5) are better at sensing gases because the depletion layer has more surface chemisorption and charge modulation.
- Larger grains with less strain (S_1, S_4) are better for coating and electrodes because they are more stable mechanically.

This study creates a model for predicting the synthesis, structure, and use of TiO_2 nanoparticles by linking the sol-gel process parameters to the functional results. This method is adaptable and applicable to doped or combined TiO_2 systems. This makes it possible to make oxides with specific electrical and catalytic properties. In the future, we will use both Raman and XPS data to confirm the Ti^{3+} defect states and the way oxygen vacancies are spread out. They will also use this information to learn more about how lattice distortion affects the electrical structure. We will also look into surface sealing and dopant tuning as ways to make photocatalysts with a high strain level, like S_0, more stable over time. In conclusion, this comparative study clarifies the influence of defects on the properties of sol-gel derived TiO_2 and formulates a comprehensive and effective design framework for the next generation of multifunctional nanomaterials.

7. ACKNOWLEDGEMENT:

The laboratory and research facilities provided by Veer Narmad South Gujarat University and N. K. Desai Science & Commerce College, Killa Pardi, are greatly appreciated by the authors. The authors also express their gratitude to colleagues and collaborators for their invaluable technical support and discussions, as well as to SAIF,

Punjab University, Chandigarh, for providing SEM and XRD characterization facilities. No funding was received to assist with the preparation of this research work and the manuscript presented.

REFERENCES:

1. Diebold U., (2003): The surface science of titanium dioxide. *Surface Science Reports*, 48, 53–229.
2. Ohtani B., (2014): Titania photocatalysis: a historical overview and future prospects. *Catalysts*, 4, 91–103.
3. Gupta S.M., and Tripathi M., (2012): A review of TiO_2 nanoparticles. *Chinese Science Bulletin*, 57, 122–137.
4. Banfield J.F., and Zhang H., (2001): Nanoparticle aggregation and growth in aqueous environments. *Reviews in Mineralogy and Geochemistry*, 44, 1–58.
5. Byrappa K., and Adschiri T., (2007): Hydrothermal technology for nanotechnology. *Progress in Crystal Growth and Characterization of Materials*, 53, 117–166.
6. Cullity B.D., and Stock S.R., (2014): *Elements of X-Ray Diffraction*, 3rd ed. Pearson Education, USA.
7. Williamson G.K., and Hall W.H., (1953): X-ray line broadening from filed aluminium and wolfram. *Acta Metallurgica*, 1, 22–31.
8. Hall W.H., (1949): The deformation and ageing of mild steel: III. Discussion of results. *Proceedings of the Physical Society London B*, 62, 741–743.
9. Spurr R.A., and Myers H., (1957): Quantitative analysis of anatase–rutile mixtures with an X-ray diffractometer. *Analytical Chemistry*, 29, 760–762.
10. Mote V.D., Purushotham Y., and Dole B.N., (2012): Williamson–Hall analysis in estimation of lattice strain in nanocrystalline TiO_2. *Journal of Theoretical and Applied Physics*, 6, 1–9.
11. Phuruangrat A., and Thongtem S., (2023): Influence of synthesis parameters on phase stability of TiO_2 nanostructures prepared by sol–gel method. *Journal of Sol-Gel Science and Technology*, 108, 65–78.
12. Ebrahimi M., and Morsali A., (2021): Influence of calcination temperature on phase transition and morphology of TiO_2 nanoparticles. *Ceramics International*, 47, 27358–27367.
13. Dhanalakshmi R., Rajarajan G., and Anandan S., (2022): Structural and photocatalytic behavior of TiO_2 nanoparticles prepared by sol–gel technique. *Journal of Sol-Gel Science and Technology*, 101, 433–445.
14. Rajput N.S., Mody K., et al., (2025): Comparative microstructural and photocatalytic evaluation of sol–gel derived TiO_2 nanoparticles. *Materials Today: Proceedings*, 92, 402–410.
15. Li H., Liu J., et al., (2024): Strain-induced band gap modulation in anatase TiO_2: insights from XRD and DFT correlation. *Materials Chemistry and Physics*, 308, 128197.
16. Liu G., et al., (2021): Multi-facet anatase TiO_2 crystals with enhanced photocatalytic and photoelectrochemical properties. *Applied Catalysis B: Environmental*, 296, 120352.
17. Kwon Y.T., et al., (2022): Synergistic role of lattice strain and surface defects in visible-light photocatalysis of TiO_2 nanoparticles. *Materials Today Chemistry*, 23, 100712.
18. Sakai N., et al., (2020): Texture coefficient analysis and facet engineering in TiO_2 thin films. *Surface and Coatings Technology*, 403, 126388.
19. Khan R., Ahmad M., et al., (2020): Defect-engineered TiO_2 nanostructures for enhanced gas sensing: correlation between defect density and sensitivity. *Applied Surface Science*, 529, 147113.
20. Zhang J., et al., (2023): Oxygen-vacancy-driven gas sensing mechanism in TiO_2 nanomaterials: linking strain and electronic structure. *Sensors and Actuators B: Chemical*, 392, 134233.
21. Choudhury B., and Choudhury A., (2014): Oxygen vacancy and dopant induced ferromagnetism in TiO_2 nanoparticles. *Materials Chemistry and Physics*, 146, 524–532.
22. Naldoni A., et al., (2012): Effect of nature and location of defects on band gap narrowing in black TiO_2 nanoparticles. *Journal of the American Chemical Society*, 134, 7600–7603.
23. Ghosh M., et al., (2023): Comparative analysis of sol–gel and hydrothermal TiO_2 nanostructures for photocatalytic H_2 generation. *Journal of Alloys and Compounds*, 938, 168824.
24. Nayak J., Sahu S., and Parida K.M., (2024): Defect chemistry of metal-oxide photocatalysts: tuning TiO_2 for visible light activity. *Advanced Materials Interfaces*, 11, 2400367.
25. Pal A., Ganguly S., Dey S., et al., (2025): Structural–defect correlation and photocatalytic behavior of sol–gel TiO_2 nanoparticles. *Ceramics International*, 51, 12501–12515.